INTERNATIONAL JOURNAL FOR NUMERICAL METHODS IN FLUIDS
Int. J. Numer. Meth. Fluids 2007; **53**:257–275
Published online 19 June 2006 in Wiley InterScience (www.interscience.wiley.com). DOI: 10.1002/fld.1280

Numerical simulation of isothermal nonwetting

C.-W. Kuo[1,‡], J.-C. Chen[1,*,†] and G. P. Neitzel[2,§]

[1]*Department of Mechanical Engineering, National Central University, Chung-Li 320, Taiwan, R.O.C.*
[2]*George W. Woodruff School of Mechanical Engineering, Georgia Institute of Technology, Atlanta, GA 30332-0405, U.S.A.*

SUMMARY

A numerical simulation of isothermal wetting suppression in the presence of shear is considered during which wetting may be prevented when a drop approaches a moving wall. Air is driven into the passage between the solid and liquid surfaces by viscous action, preventing wetting. Silicone-oil and water drops are investigated for different wall velocities and wall distances. The droplet dimples at the upstream side and bulges at the downstream side when nonwetting occurs. The free-surface deformation can be enlarged by either increasing the wall velocity or decreasing the wall distance. The low-viscosity silicone-oil used in these calculations is much more sensitive to shear wetting suppression than is water, because the Weber number of the silicone-oil is larger than that of water. Copyright © 2006 John Wiley & Sons, Ltd.

Received 28 October 2005; Revised 18 April 2006; Accepted 19 April 2006

KEY WORDS: noncoalescence; isothermal nonwetting; droplet; free-surface deformation

1. INTRODUCTION

Noncoalescing and nonwetting behaviours driven by hydrodynamic lubrication have recently been reviewed by Neitzel and Dell'Aversana [1]. The apparent contact without coalescence between droplets of the same liquid and suppression of wetting for droplets approaching a surface can be attributed to the existence of an intervening gas film. Noncoalescing and nonwetting states can be classified in terms of the temporal state, i.e. temporary versus permanent, and also by the nature of the repulsive force, i.e. fluid dynamic, electrostatic charge, van der Waals attraction, or DLVO (interactions resulting from the combination of van der Walls attraction and double-layer

*Correspondence to: J.-C. Chen, Department of Mechanical Engineering, National Central University, Chung-Li 320, Taiwan, R.O.C.
†E-mail: jcchen@cc.ncu.edu.tw
‡E-mail: kuocw00@yahoo.com.tw
§E-mail: paul.neitzel@me.gatech.edu

Contract/grant sponsor: Office of Biological and Physical Research of NASA

repulsion) [1]. This study focuses on permanent nonwetting caused by fluid-dynamic forces. In the case of permanent noncoalescence (nonwetting), lubricating fluid does not drain away but is continuously replenished by controlling either the temperature difference between the liquid (liquid/solid) surfaces or the relative tangential speed between droplet and bath (solid surface). In the first case, thermocapillary (or Marangoni) stress, which is induced by the temperature-induced surface-tension gradient, continuously supplies refresh lubricant, separating the noncoalescing or nonwetting surfaces. This phenomenon has been called 'self-lubrication.' In the second case, forced relative tangential motion is used to supply the lubricating gas via the no-slip condition. It is this second case, in particular applied to a nonwetting situation, which is the focus of the present work.

The observation of bouncing droplets by Rayleigh [2] was the first systematic investigation of temporary noncoalescense. The phenomenon is due to competition between the time scales associated with the draining of lubricating gas between the liquid surfaces and the restoring surface-tension forces.

The first report of permanent, thermocapillary-induced noncoalescense was by Napolitano *et al*. [3], in which they reported difficulty re-connecting two ends of a nonisothermal, liquid bridge broken during a space experiment. Renewed interest in these subjects is due to experiments performed by Dell'Aversana and co-workers [4, 5] that demonstrate permanent noncoalescense and nonwetting. Some of this interest is due to the potential for applications of the phenomena in the form of bearings and springs, or for the enhancement of droplet transport, in low-load environments. Further examples and discussion are provided in the review by Neitzel and Dell'Aversana [1]. A paper by Dell'Aversana and Neitzel [6] discusses both noncoalescing and nonwetting states, including the possible failure of the lubricating film. Sumner *et al*. [7] treat a two-dimensional, thermocapillary nonwetting case using lubrication theory and a recent paper by the present authors [8] explores numerical solutions for this case.

Neitzel and Dell'Aversana [1] have presented preliminary results showing that a solid surface with sufficient tangential velocity is capable of avoiding wetting by an approaching droplet at the same temperature as the surface. The free surface of such an isothermal, nonwetting drop exhibits a dimple, which deepens and widens with an increase of the load. Such droplets are able to slide across the moving surface with minimal friction. Experiments provide a wealth of information about such systems; however, design efforts would be enhanced by the availability of a numerical model that can faithfully simulate such behaviour. The purpose of the present work is to demonstrate a simulation capability for a two-dimensional, isothermal nonwetting droplet.

Simulations of a nonwetting droplet are complicated by the disparate length scales associated with flows within the gas and liquid fields: typical droplet sizes in experiments are of $O(\text{mm})$ while film thicknesses are $O(\mu\text{m})$. Previous numerical simulations have treated the gas phase in an *ad hoc* manner, such as those of Monti *et al*. [9, 10] in which the lubricating film is modelled as a duct flow within an axisymmetric channel. A recent paper by Smith and Neitzel [11] has discussed a multi-scale model of isothermal nonwetting with a hybrid approach employing lubrication theory for the interstitial film and numerical simulation for the liquid and outer gas fields. In this approach, the net flow rate in the channel must be specified as the known condition. As noted briefly above numerical simulation of thermocapillary wetting suppression has been performed by the present authors [8] using the commercial code FIDAP, which is also the approach taken for the present work. In this paper, flows in the liquid and gas phases are computed simultaneously, adjusting the interface position through the use of the stress boundary conditions imposed thereon. Their results have shown that thermocapillary nonwetting can occur when either a silicone-oil or water drop approaches a cold wall. The region of 'apparent contact' can be enlarged by either increasing

DOI: 10.1002/fld

the temperature difference or decreasing the relative distance between the wall and the drop. The silicone-oil drop has a higher Capillary number than that of water, so the nonwetting effect is easier to obtain with the former.

In the present study, we perform a numerical simulation of two-dimensional, isothermal nonwetting using the commercial code FIDAP, based on finite-element techniques. The physical problem considered here is a two-dimensional liquid drop attached to a fixed wall and pressed against a wall sliding with constant speed normal to the direction along which the droplet is pressed. The flows in both the gas and liquid phases are computed simultaneously in order to investigate the nonwetting phenomenon.

2. MATHEMATICAL FORMULATION

Two parallel solid walls are separated by a distance D. A two-dimensional semicircular drop of radius R of an incompressible, Newtonian liquid is attached to the fixed wall, while the other moves with a constant velocity V in the negative x-direction, as shown in Figure 1. The drop is surrounded by air. The vertex point of the drop has the minimum proximity to the opposing solid surface, and a thin air film separates the liquid and solid surfaces. A continuum model with a no-slip boundary condition is assumed for the gas phase since the Knudsen number $Kn = \lambda/\delta$ is less than 10^{-2} [6], where λ is the mean free path of air and δ is the thickness of the lubricating film of air. Usually, the drops in the experiments [4, 5] are formed by injecting liquid from a reservoir through a hole or slot in the sharp-edged disk to which the droplet is affixed. The droplet spreads along the flat surface and the contact line becomes pinned to the sharp edge of the disk. In Reference [6], the

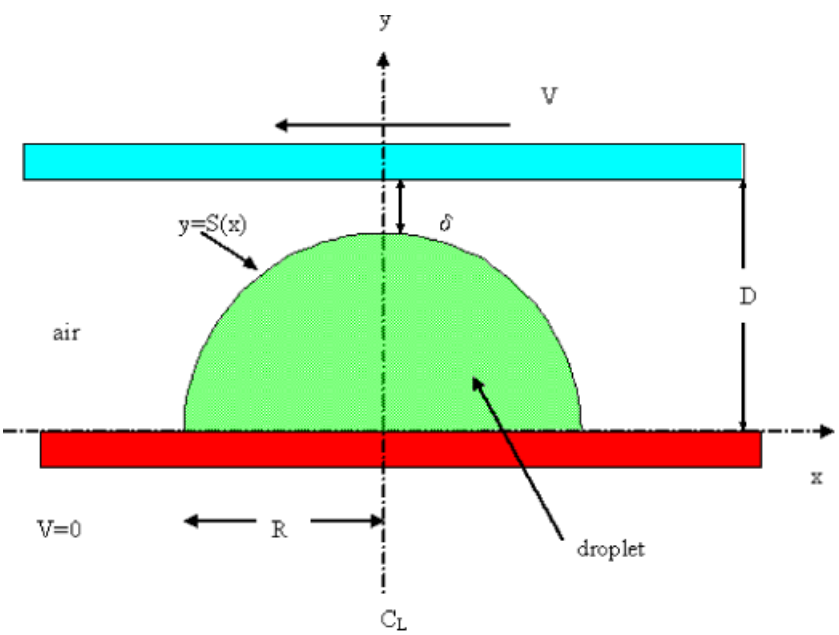

Figure 1. Physical model of the simulation.

DOI: 10.1002/fld

pinning of contact line to this edge is enhanced by applying a barrier-wetting agent to the entire disk. We have selected a channel domain for simplicity, choosing to focus on the effect of the lubrication region and free-surface deformation. Therefore, to simulate the disk geometry of the experiments, the contact lines in the present calculations are assumed to be pinned at $x = \pm R$ on the lower surface. The drop sizes considered in the present computations are $O(\text{mm})$, so the liquid volume is small and the Bond number $Bo = \rho_1 g R^2/\gamma_1$ is less than unity, where ρ_1, γ_1, R are the density, surface tension, and radius of droplet, respectively, and g is the gravitational acceleration. Hence, gravity may be safely neglected in these computations.

The governing equations for this model are the continuity, and Navier–Stokes equations:

$$\nabla \cdot \mathbf{V}_i = 0 \tag{1}$$

$$\rho_i[(\mathbf{V}_i \cdot \nabla)]\mathbf{V}_i = -\nabla \boldsymbol{P}_i + \mu_i \nabla^2 \mathbf{V}_i \tag{2}$$

where $\mathbf{V}_i = u_i \mathbf{i} + v_i \mathbf{j}$ is the velocity vector, P_i is the pressure, ρ_i is the density, and μ_i is the dynamic viscosity. The subscript 'i' = 'l' denotes the liquid phase ('l' = 's' if the liquid is silicone-oil; 'l' = 'w' if the liquid is water) and 'i' = 'a' represents a air.

The gas–liquid interface described by $y = S(x)$ satisfies the kinematic, stress continuity, and no-slip conditions at the interface:

$$\mathbf{V}_\mathrm{l} \cdot \nabla S = \mathbf{V}_\mathrm{a} \cdot \nabla S \tag{3}$$

$$\boldsymbol{\sigma}_\mathrm{l} - \boldsymbol{\sigma}_\mathrm{a} = 2\gamma_\mathrm{l} H - \nabla \gamma_\mathrm{l} \tag{4}$$

$$\mathbf{V}_\mathrm{l} = \mathbf{V}_\mathrm{a} \tag{5}$$

where H is the mean curvature of the surface, $\boldsymbol{\sigma}_i$ is the stress vector, and the surface tension of a particular liquid is γ_l. The boundary conditions on the solid surfaces are the kinematic and no-slip conditions, and both the stress in x-direction and the y-component of velocity are constrained to be zero as the boundary conditions of the entrance and exit:

$$u_\mathrm{a} = V, \quad v_\mathrm{a} = 0 \quad \text{for } y = D \text{ and } -\infty \leqslant x \leqslant \infty \tag{6}$$

$$u_i = v_i = 0 \quad \text{for } y = 0 \text{ and } -\infty \leqslant x \leqslant \infty \tag{7}$$

$$\frac{\partial u_\mathrm{a}}{\partial x} = v_\mathrm{a} = 0 \quad \text{for } |x| \to \infty \text{ and } 0 < y < D \tag{8}$$

The drop is assumed to be pinned to the fixed wall at $x = \pm R$, i.e. the contact line is fixed, requiring that

$$S(-R) = S(R) = 0 \tag{9}$$

Finally, the droplet's volume is conserved, requiring

$$\int_{-R}^{R} S(x)\,\mathrm{d}x = \Gamma \tag{10}$$

where Γ is the drop volume per unit length normal to the plane of the figure.

The above continuum equations and boundary conditions are discretized by the Galerkin finite-element method (GFEM), and the resulting nonlinear algebraic equations then solved using the

DOI: 10.1002/fld

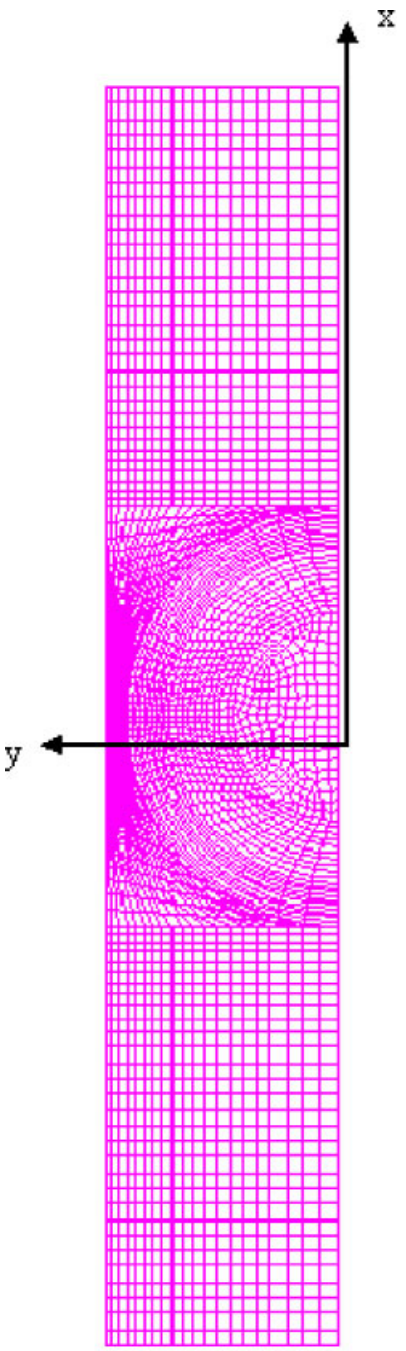

Figure 2. Mesh configuration of the physical domain.

DOI: 10.1002/fld

uncoupled (i.e. segregated solver) method employed in the commercial code FIDAP. Each degree of freedom is solved separately. The normal-stress balance condition is utilized to update the position of the free surface for each iteration. The solution obtained is checked for velocity convergence within a preset tolerance (less than 10^{-6}) being satisfied, based on the criterion of solution-vector relative error. A discontinuous pressure approximation combined with a mixed method is used and upwinding is employed to prevent wiggles. Spatial instability appears as node-to-node overshoots or undershoots in the solution variables. The complex geometries of the physical domain (Figure 1) are handled with unstructured quadrilateral simplex elements. To address the difficulty of disparate length scales associated with droplet and interstitial film, an appropriate finer mesh is applied near the free surface in both liquid and gas fields; the nodes on the free surface are permitted to move in the direction of the local normal. The mesh plot is illustrated in Figure 2. Test computations of mesh convergence were performed by increasing the element number on all domains and boundaries, until the quantitative variations, i.e. the maximum and minimum velocity, pressure, and radius on the droplet free surface, were less than 0.5%, which was regarded as an acceptable accuracy. For different sets of finite elements, the results showed that the use of 3310 elements yields both acceptable accuracy and computation time.

3. RESULTS AND DISCUSSION

In the present simulation, the liquid inside a semicircular drop with $R = 1$ mm is selected to be either 5 cSt silicone-oil or water; their physical properties are listed in Table I. Isothermal noncoalescence [4] and nonwetting [6] experiments evaluated the phenomena with surfaces moving from 350 to 450 mm/s and showed lateral vertex displacements for millimeter-sized droplets of hundreds of microns for squeezing on the order of 10 μm. Therefore, the wall speeds, $V = 300$, 400, and 500 mm/s, as well as the distances between two walls, $D = 1.01$, 1.03, and 1.05 mm, are chosen in this study.

Figure 3 displays the streamlines and velocity vectors for silicone-oil, with $V = 300$ mm/s and $D = 1.01$ mm. In what follows, the direction of wall motion will be referred to as the 'downstream' direction. The air close to the moving wall flows downstream, induced by viscous forces. Part of the gas passes through the gap between the wall and droplet, while the rest impinges on the droplet surface, flowing along it toward the support, finally moving upstream due to a pressure gradient established by the blocking of the flow by the droplet. Therefore, the velocity vectors at the entrance (Figure 3(b)) to the computational domain exhibit a two-dimensional Couette–Poiseuille-type profile. In the lubricating film, the gas velocity decreases from the moving-wall velocity to the droplet velocity at the interface (Figure 3(c)). After the air passes through the thinnest portion of the film, it decelerates due to the widening gap. Interestingly, the air flow in the downstream portion of the geometry exhibits a similar behaviour to that on the

Table I. Fluid material properties.

	ρ (kg/m^3)	γ (kg/s^2) at 20°C	μ (kg/m/s)
Silicone-oil	9.1×10^2	1.92×10^{-2}	4.55×10^3
Water	9.98×10^2	7.27×10^{-2}	1.002×10^3
Air	1.21		1.528×10^5

DOI: 10.1002/fld

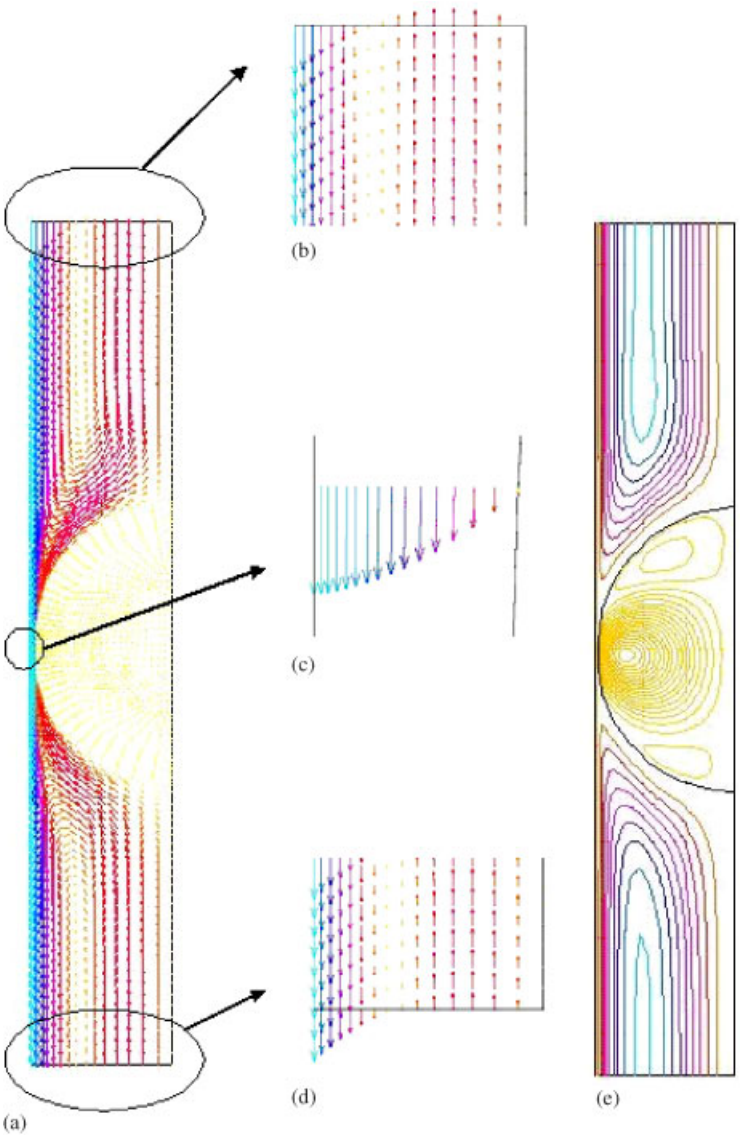

Figure 3. (a) Velocity vector field; (b) entrance field; (c) velocity vector of lubricating film; (d) exit field; and (e) streamline contours for $V = 300\,\mathrm{mm/s}$ and $D = 1.01\,\mathrm{mm}$.

upstream side, moving upstream along the fixed wall, flowing around the droplet's free surface, merging with the air which constitutes the lubricating film, and finally flowing toward the exit (Figure 3(d)). Defining the flow rate in the gas as $q = \int u_a \, dy$, the constant values of q $(= 2.463\,\mathrm{mm}^2/\mathrm{s})$ at entrance, lubricating film and exit, identify the mass conservation of the present simulation.

DOI: 10.1002/fld

There are three vortices inside the droplet, as indicated by the streamlines of Figure 3(e). The major vortex appears in the droplet centre, and the other two vortices are located at the upstream and downstream sides of the droplet. The strength of the upstream side corner vortex is stronger than that on the downstream side, and these two corner vortices rotate in a direction opposite to that of the major, central one. The counter-clockwise flow motion of the major vortex is induced by the increased air velocity within the interstitial film. The streamlines for the flow field from the multiscale model of Smith and Neitzel [11] computed for $V = 300\,\text{mm/s}$, $D = 1.01\,\text{mm}$ and $q = 2.491\,\text{mm}^2/\text{s}$ are similar to those seen in Figure 3(e).

Figure 4 exhibits the resultant speed ($V_s = \sqrt{u^2 + v^2}$), and pressure-difference ($\Delta P = P_a - P_l$) distribution on the silicone-oil drop's free surface, when the wall's distance is fixed ($D = 1.01\,\text{mm}$) and the moving-wall velocity is varied ($V = 300$, 400, and 500 mm/s). The positive value of resultant velocity is defined for the counter-clockwise flow motion along the free surface, and the negative one for the clockwise flow motion. The speed distribution (Figure 4(a)) shows two stagnation points ($V_s = 0$) located near $x = 0.35\,\text{mm}$ and $x = -0.6\,\text{mm}$ when $V = 300\,\text{mm/s}$, while those of Smith and Neitzel [11] are located at $x = -0.4\,\text{mm}$ and $x = 0.75\,\text{mm}$. In this case, the maximum speed is $V_s = 11.61\,\text{mm/s}$ located at $x = -0.06\,\text{mm}$, while Smith and Neitzel [11] show $V_s = 12.57\,\text{mm/s}$ at $x = -0.069\,\text{mm}$, an 8.3% resultant velocity difference. These results indicate that those from the two models agree quite well.

The pressure-difference distribution on the free surface (Figure 4(b)) shows two local maxima located near $x = 0.2\,\text{mm}$ and $-0.15\,\text{mm}$, but these are not stagnation points. The positions of these local maxima move slightly downstream as V increases. The upstream local maximum increases with V due to the effect of faster-moving air impinging on the free surface. The pressure difference exhibits a local minimum between $x = 0.2\,\text{mm}$ and $x = -0.15\,\text{mm}$, due to the increased speed within the film at the point of minimum thickness (Figure 4(a)) and then increases to the second local maximum. Also observed in Figure 4(b) are the upstream and downstream negative pressure gradients that drive the flows in the upstream direction along the stationary wall.

Figure 5 presents results of calculations performed for water under the same conditions of displacement and wall speed used for the silicone-oil computations of Figure 4. The trend for water drops is similar to that for silicone-oil drops. The Reynolds number is defined as $Re_l = \rho_l V R/\mu_l$, and is a measure of inertial force to viscous force. At $V = 300\,\text{mm/s}$, the Reynolds number of a water droplet ($Re_w = 298.8$) is much larger than that of a corresponding silicone- oil droplet ($Re_s = 60$). Hence, the free-surface velocity of water (Figure 5a) is much larger than the corresponding one for silicone-oil (Figure 4(a)). In turn, this makes the pressure difference for water (Figure 5(b)) greater than that for silicone-oil (Figure 4(b)).

The effect of distance between the droplet and moving wall has also been examined. Figure 6 displays the influence of distance ($D = 1.01$, 1.03, and 1.05 mm) for silicone-oil droplets when the moving-wall velocity is constant ($V = 300\,\text{mm/s}$). The free-surface velocity plot (Figure 6(a)) shows, not surprisingly, that the maximum velocity increases with decreasing film thickness (smaller D). The pressure difference is also affected by the variation of the wall distance, as shown in Figure 6(b). The air driven by the wall motion impinges on the upstream side of the droplet. On the other hand, the air impingement on the downstream side is induced by the recirculating flow, owing to the requirement of mass conservation. It is obvious that both impinging effects increase as D decreases. Therefore, as D is reduced, the local maxima of the pressure values increase. When $D = 1.01\,\text{mm}$, the impingement on the upstream side of the droplet is greater than that on the downstream side. For larger gaps, this trend is reversed. The higher local maximum pressure difference for $D = 1.01\,\text{mm}$ occurs at the upstream side, while that for $D = 1.03$ and 1.05 mm

DOI: 10.1002/fld

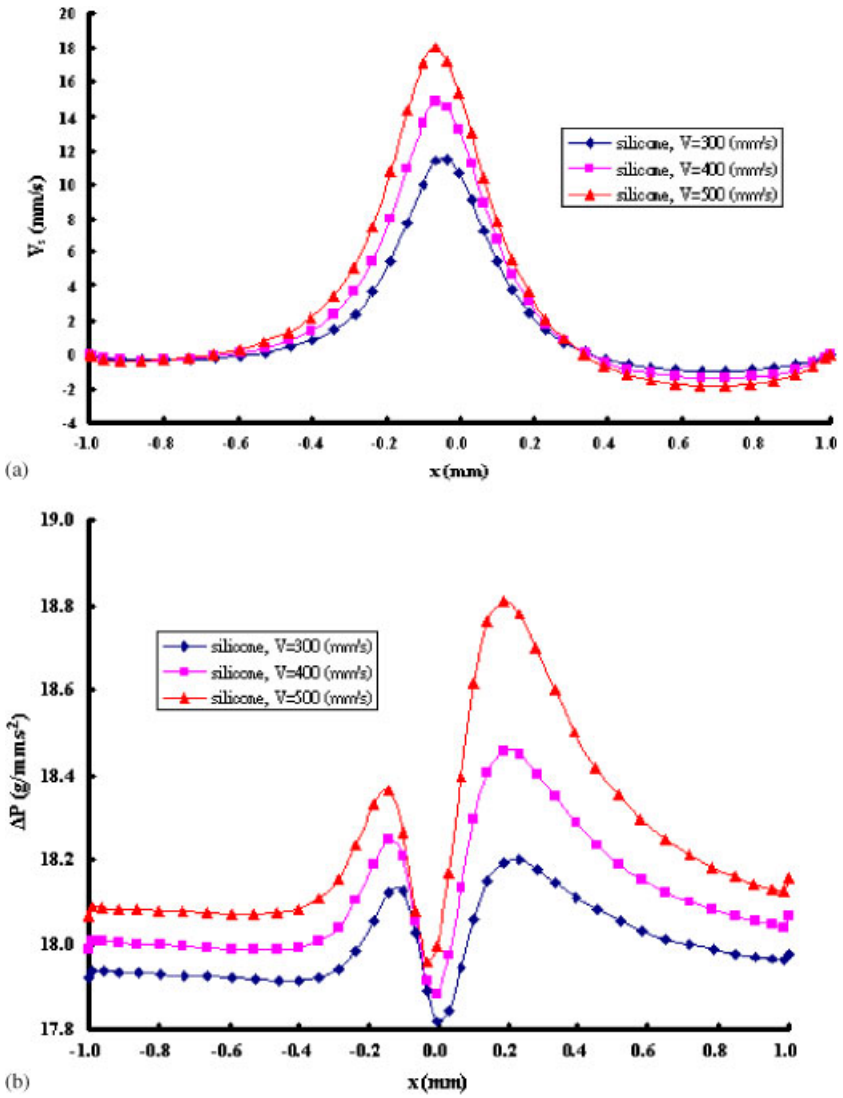

Figure 4. (a) Free-surface speed; and (b) pressure difference versus x for a silicone-oil drop with $D = 1.01$ mm and three different V.

appears downstream. The consequence of a different squeezing ($D = 1.01$, 1.03, and 1.05 mm) for the water drop (for $V = 300$ mm/s) is illustrated by Figure 7. The trends of the free-surface velocity and pressure-difference distributions for water are similar to those for silicone-oil.

Experimental investigations [1] of sliding droplets have revealed film shapes that exhibit a dimpled region that terminates in a bulge near the downstream side of the droplet (see, e.g. Reference [1, Figure 10]). Figure 8(a), showing the local free-surface radius $r(x)$ versus x, illustrates how the variation of the moving-wall velocity influences the deformation of a silicone-oil drop,

DOI: 10.1002/fld

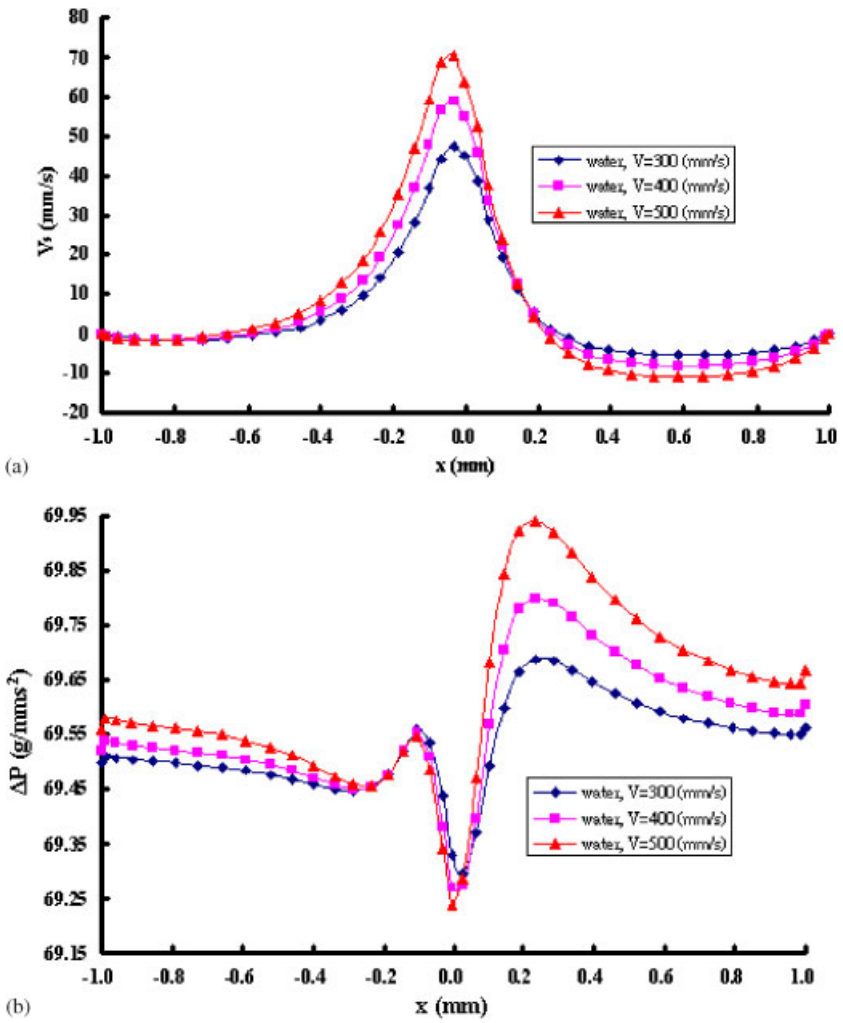

Figure 5. (a) Free-surface speed; and (b) pressure difference versus x for a water drop with $D = 1.01$ mm and three different V.

for $D = 1.01$ mm. The free surface dimples on the upstream side and bulges on the downstream side; in addition, the deformation is amplified as the wall speed increases. Figure 8(b) shows the net normal stress σ_n acting on the silicone-oil free surface as a function of x. The maximum net normal stress occurs at roughly $x = 0.2$ mm, and then decreases rapidly to a minimum value at about $x = -0.2$ mm; this means that the upstream side endures more net normal stress than the downstream side. Additionally, the drop's volume must be conserved, requiring that the upstream side be concave and the downstream side convex. Moreover, increasing moving-wall velocity increases the net normal stress over the droplet surface. This is especially apparent at the upstream side. Equation (4) shows that the mean curvature is proportional to the net normal stress. This explains why at the upstream side, the smaller radius (Figure 8(a)) (i.e. larger curvature) corresponds

DOI: 10.1002/fld

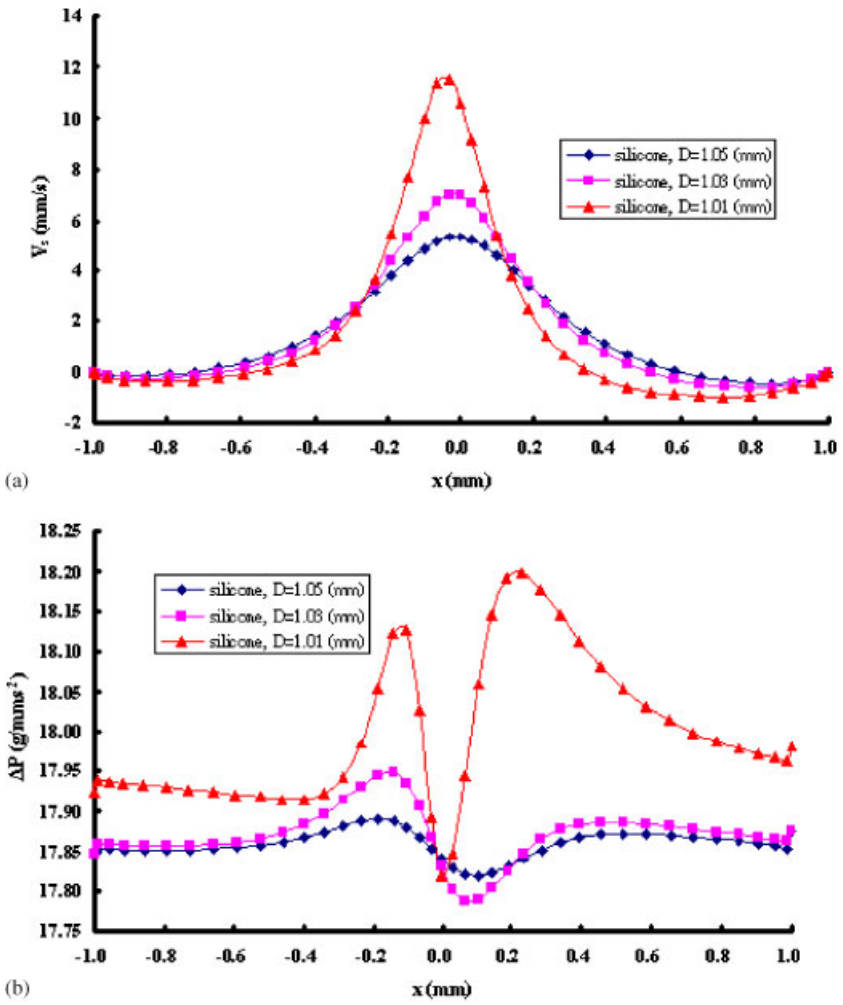

Figure 6. (a) Free-surface speed; and (b) pressure difference versus x for a silicone-oil drop with $V = 300\,\text{mm/s}$ and three different D.

to the greater net normal stress (Figure 8(b)). Consequently, conservation of droplet volume requires that the smaller radius at the upstream side be balanced by a greater radius (smaller curvature) on the downstream side.

The net tangential stress σ_t acting on the free surface is plotted (Figure 8(c)). It shows that the maximum net tangential stress occurs near $x = 0$, explaining the free-surface velocity peak there. Far away from the vertex, on both sides, there are negative values, which represent upstream motion. As the moving-wall velocity increases, the positive value increases and the negative value decreases.

Figure 9 shows the droplet radius, net normal stress, and net tangential stress for a water droplet for varying moving-wall speed and constant D. Again, the trends observed for water droplets are similar to those seen for silicone-oil droplets.

DOI: 10.1002/fld

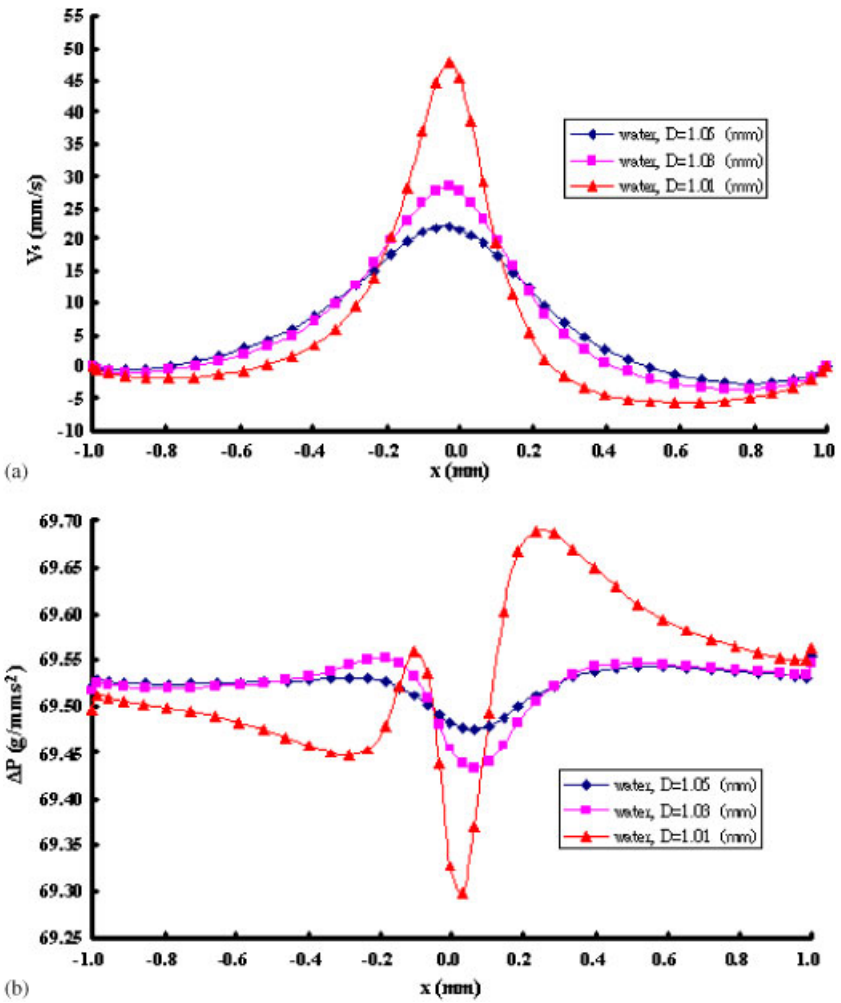

Figure 7. (a) Free-surface speed; and (b) pressure difference versus x for a water drop with $V = 300\,\mathrm{mm/s}$ and three different D.

The influence of squeezing (i.e. varying D) on radius, normal stress and tangential stress is illustrated in Figure 10 for a silicone-oil droplet and fixed wall speed of $V = 300\,\mathrm{mm/s}$. The amount of deformation clearly increases with increased squeezing. Whereas the results of Figure 8(b) show an increase in the local normal stress for all values of x with increasing wall speed V, the results in Figure 10(b) indicate a deepening of the minimum 'well' in normal stress near $x = -0.2\,\mathrm{mm}$ with increased squeezing. Trends in the shear stress are similar to those exhibited for increasing V.

Figure 11 displays the free-surface distributions of the water's radius, the net normal stress, and the net tangential stress, for the same conditions as presented for silicone-oil in Figure 10. The trends for water are similar to those for silicone-oil.

DOI: 10.1002/fld

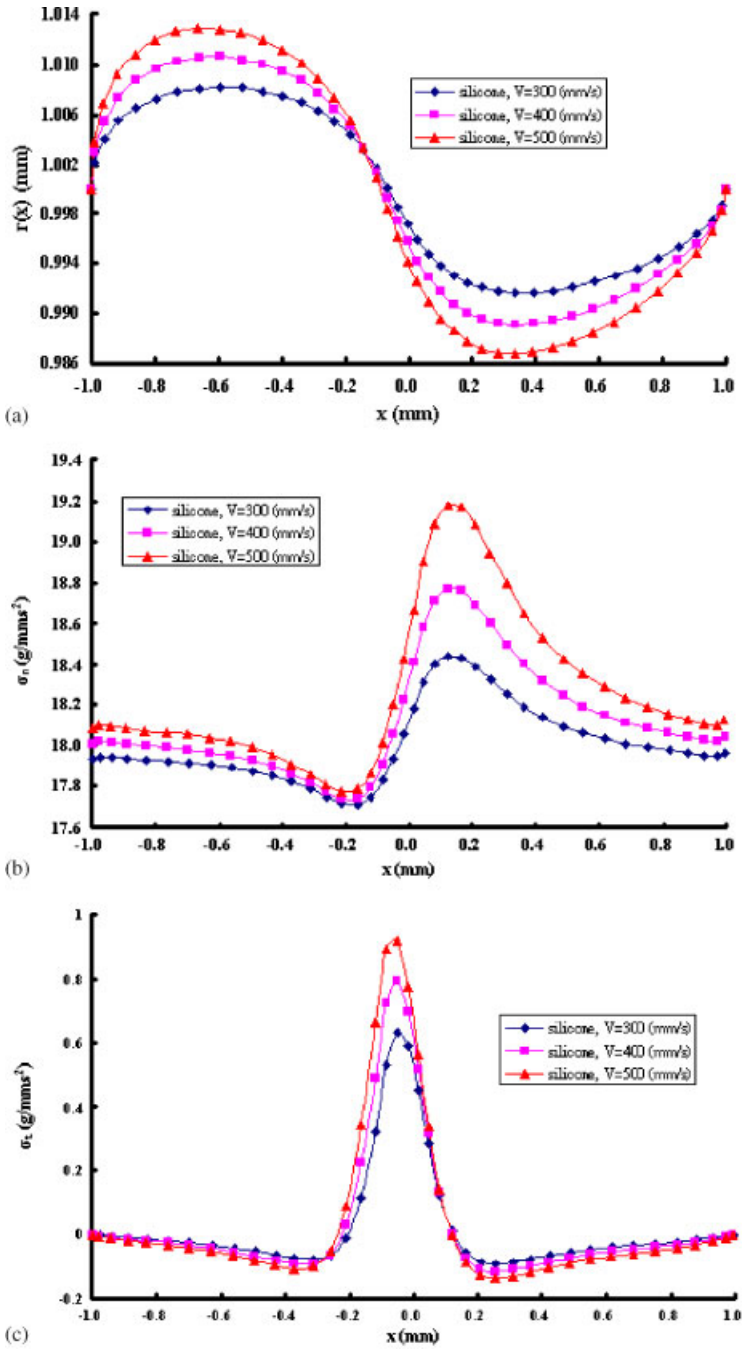

Figure 8. (a) Drop radius; (b) net normal stress; and (c) net tangential stress versus x for a silicone-oil drop with $D = 1.01$ mm and three different V.

DOI: 10.1002/fld

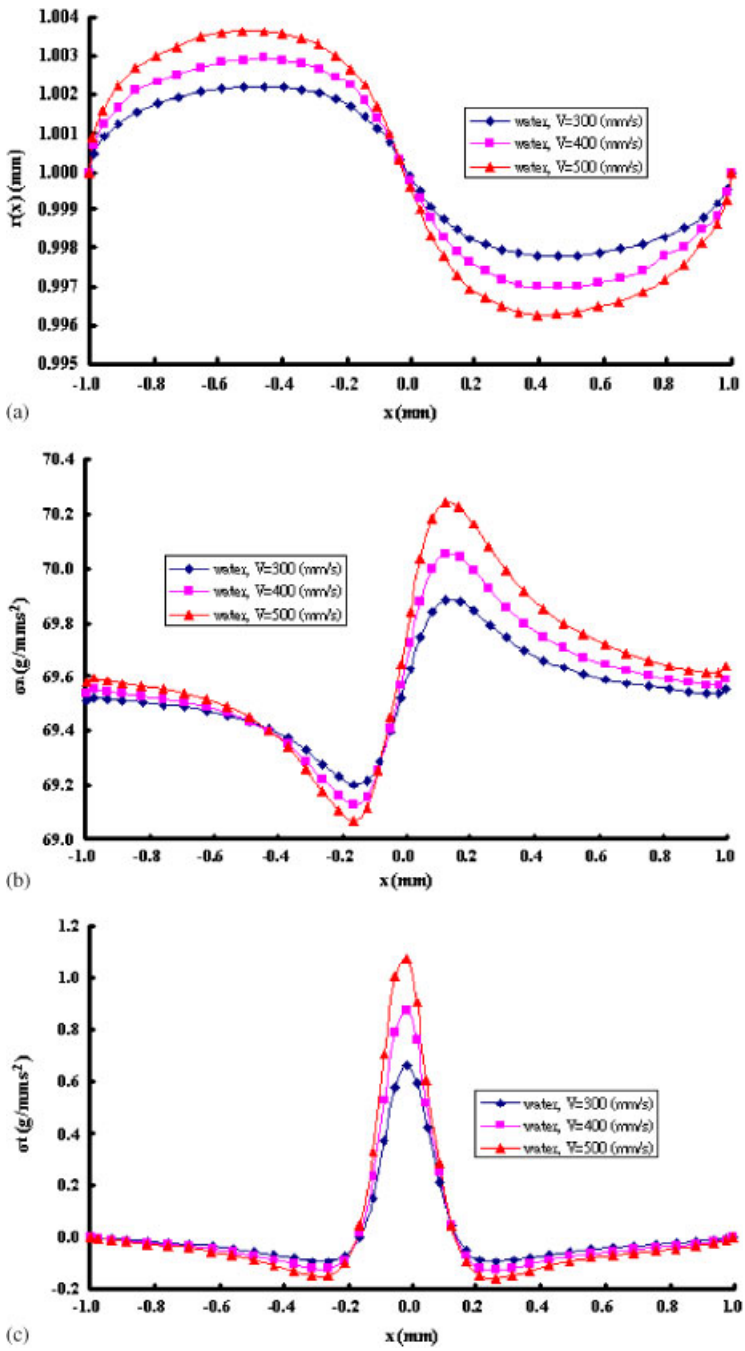

Figure 9. (a) Drop radius; (b) net normal stress; and (c) net tangential stress versus x for a water drop with $D = 1.01$ mm and three different V.

DOI: 10.1002/fld

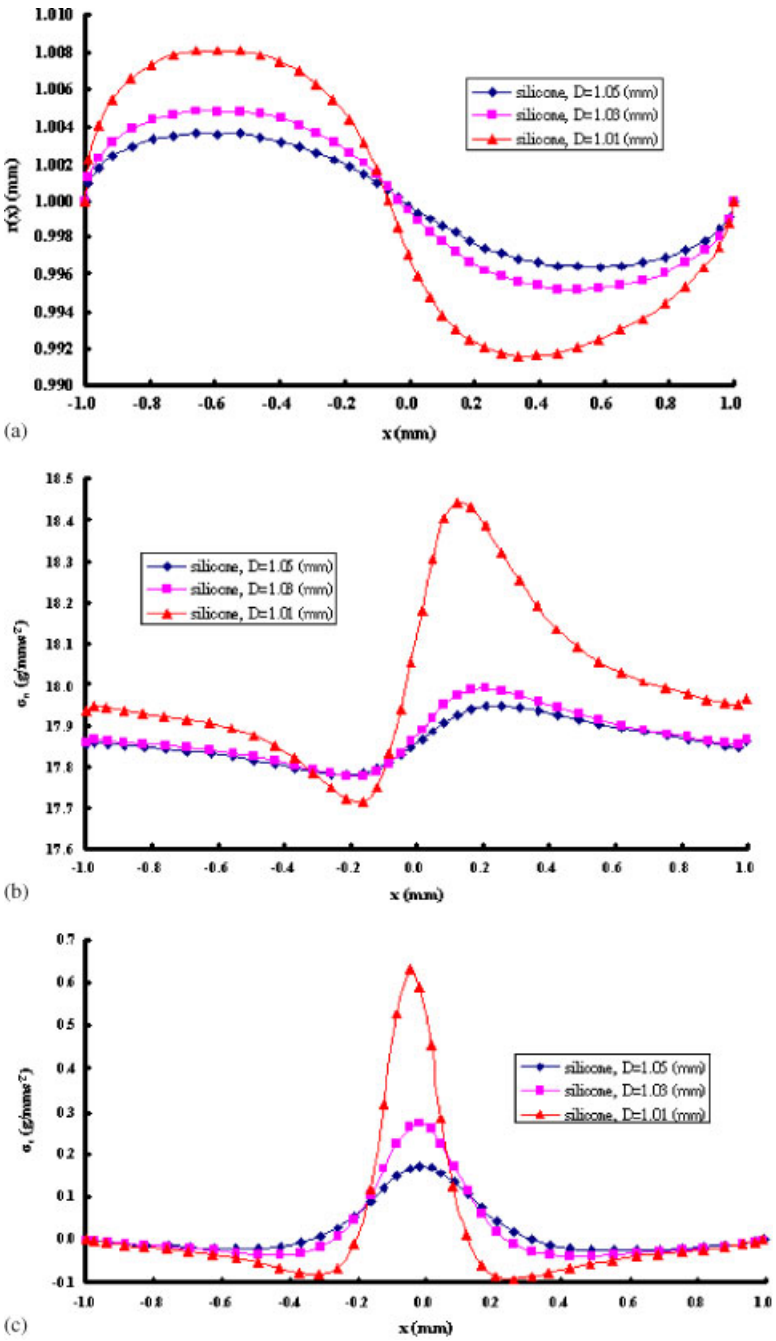

Figure 10. (a) Drop radius; (b) net normal stress; and (c) net tangential stress versus x for a silicone-oil drop with $V = 300\,\text{mm/s}$ and three different D.

DOI: 10.1002/fld

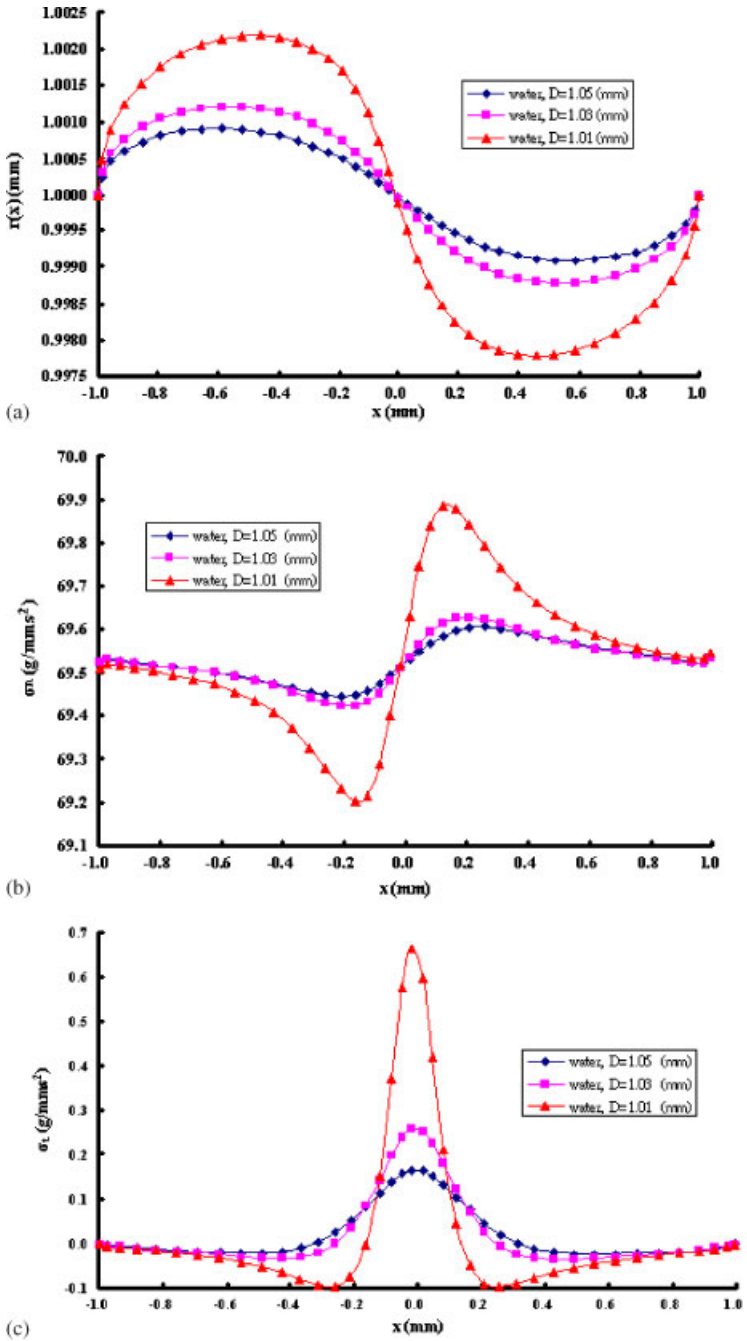

Figure 11. (a) Drop radius; (b) net normal stress; and (c) net tangential stress versus x for a water drop with $V = 300\,\text{mm/s}$ and three different D.

DOI: 10.1002/fld

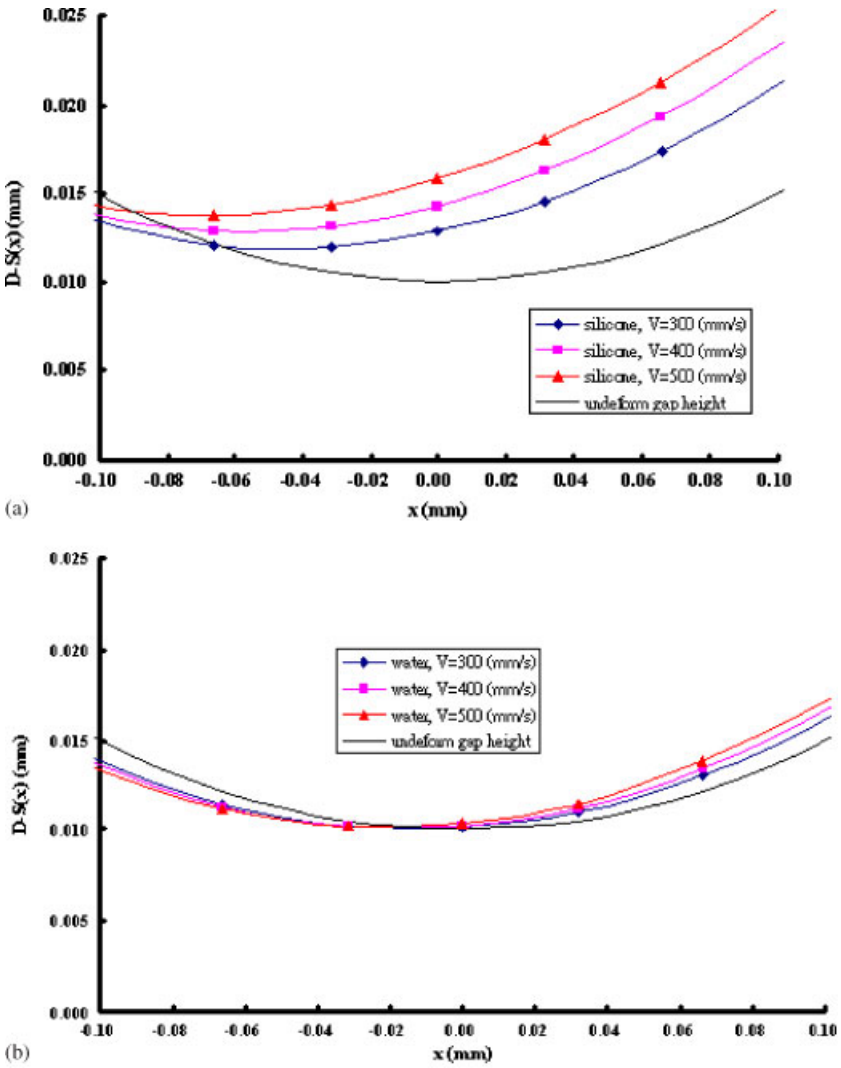

Figure 12. Interstitial film height $D - S(x)$ versus x for three different V of: (a) silicone-oil drop; and (b) water drop.

In order to gain a better understanding of how the moving-wall velocity influences the non-wetting near the vertex ($-0.1<x<0.1$), the film thickness is defined as $D - S(x)$. Figure 12 shows the behaviour of $D - S(x)$ versus x for different wall velocities for both silicone-oil and water; the results show the free surface being depressed upstream and bulging downstream, compared with the undeformed profile. For $V = 300\,\text{mm/s}$, the minimum interstitial film is 0.012 mm at $x = -0.05\,\text{mm}$, while Smith and Neitzel [11] reported minimum film being 0.0122 mm at $x = -0.073\,\text{mm}$. The Weber number is the ratio of inertial force to surface-tension force, defined for the present situation as $We_1 = \rho_1 V^2 R/\gamma_1$, and is indicative the degree of surface deformation.

DOI: 10.1002/fld

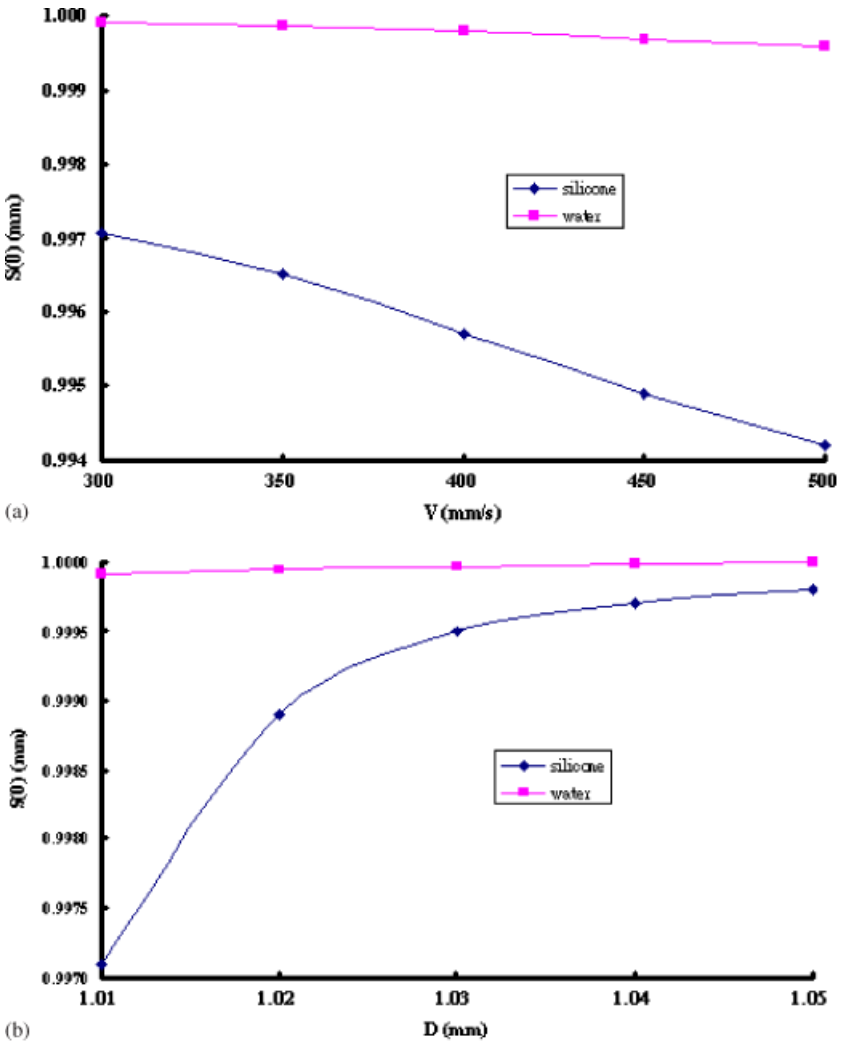

Figure 13. (a) $S(0)$ of silicone-oil and water drop versus V with $D = 1.01$ mm; and (b) $S(0)$ of silicone-oil and water drop versus D with $V = 300$ mm/s.

For $V = 500$ mm/s with $D = 1.01$ mm, the Weber number of water is $We_{\mathrm{w}} = 3.43$, much less than that of silicone-oil ($We_{\mathrm{s}} = 11.85$), due to water's large surface tension. Therefore, the deformation of the water droplet from its undeformed position is small in comparison with that observed for silicone-oil. Consequently, the nonwetting effect is likely easier to observe for silicone-oil droplets due to their greater deformability. This is further illustrated in Figure 13, which shows the effect of wall speed (Figure 13(a)) and squeezing (Figure 13(b)) on the height of the surface at $x = 0$. Increased squeezing and wall speed more profoundly impact $S(0)$ for silicone-oil than water.

DOI: 10.1002/fld

4. SUMMARY

The simulations described above demonstrate the effects of wall speed and squeezing on the deformation of two-dimensional silicone-oil and water droplets attached to fixed walls and pressed toward moving ones, explaining how the establishment of a lubricating film of surrounding fluid can prevent the liquid and solid surfaces from coming into contact. The results show that film deformation increases with both wall speed and squeezing for both water and silicone-oil droplets, with greater deformation for a given wall speed and squeezing observed for silicone-oil because of its larger Weber number. Although deformation certainly contributes to the establishment of nonwetting states, excessive deformation can lead to wetting events.

Such simulations may be of assistance in determining conditions under which isothermal nonwetting systems may be prone to failure. Likewise, simulations can be helpful in determining the influence of surface contaminants that either increase (e.g. surfactants) or decrease (e.g. dust) surface mobility. Such influences are important to understand if nonwetting systems are to be exploited technologically.

ACKNOWLEDGEMENTS

GPN was supported by a grant from the Office of Biological and Physical Research of NASA.

REFERENCES

1. Neitzel GP, Dell'Aversana P. Noncoalescence and nonwetting behavior of liquids. *Annual Review of Fluid Mechanics* 2002; **34**:267–289.
2. Rayleigh L. The influence of electricity on colliding water drops. *Proceedings of the Royal Society of London, Series A* 1879; **28**:406–409.
3. Napolitano L, Monti R, Russo G. Marangoni convection in one- and two-liquids floating zones. *Naturwissenschaften* 1986; **73**:352–355.
4. Dell'Aversana P, Banavar JR, Koplik J. Suppression of coalescence by shear and temperature gradients. *Physics of Fluids* 1996; **8**:15–28.
5. Dell'Aversana P, Tontodonato V, Carotenuto L. Suppression of coalescence and of wetting: the shape of the interstitial film. *Physics of Fluids* 1997; **9**:2475–2485.
6. Dell'Aversana P, Neitzel GP. Behavior of noncoalescing and nonwetting drops in stable and marginally stable states. *Experiments in Fluids* 2004; **38**:299–308.
7. Sumner LBS, Wood AM, Neitzel GP. Lubrication analysis of thermocapillary induced nonwetting. *Physics of Fluids* 2003; **15**:2923–2933.
8. Chen JC, Kuo CW, Neitzel GP. Numerical simulation of thermocapillary nonwetting. *International Journal of Heat and Mass Transfer*, 2006, in press.
9. Monti R, Savino R. Correlation between experimental results and numerical solutions of the Navier–Stokes problem for noncoalescing liquid drops with Marangoni effects. *Physics of Fluids* 1997; **9**:260–262.
10. Monti R, Savino R, Lappa M, Tempesta S. Behavior of drops in contact with pool surfaces of different liquids. *Physics of Fluids* 1998; **10**:2786–2796.
11. Smith MK, Neitzel GP. Multiscale modeling in the numerical computation of isothermal nonwetting. *Journal of Fluid Mechanics* 2006; **554**:67–83.

DOI: 10.1002/fld